promoting access to White Rose research papers

Universities of Leeds, Sheffield and York
http://eprints.whiterose.ac.uk/

This is the author's post-print version of an article published in the **Journal of Chemical Physics**

White Rose Research Online URL for this paper:

http://eprints.whiterose.ac.uk/id/eprint/76462

Published article:

Plane, JM, Whalley, CL, Frances-Soriano, L, Goddard, A, Harvey, JN, Glowacki, DR and Viggiano, AA (2012) *O2(a1Δg) + Mg, Fe, and Ca: experimental kinetics and formulation of a weak collision, multiwell master equation with spin-hopping.* Journal of Chemical Physics, 137 (1). 014310.

http://dx.doi.org/10.1063/1.4730423

White Rose Research Online
eprints@whiterose.ac.uk

$O_2(a\ ^1\Delta_g)$ + Mg, Fe, and Ca: experimental kinetics and formulation of a weak collision, multiwell master equation with spin-hopping

J. M. C. Plane,[1]* C. L. Whalley,[1] L. Soriano,[1,2] A. Goddard,[1] J.N. Harvey,[3] D. Glowacki,[3]* and A. A. Viggiano[4]

[1] School of Chemistry, University of Leeds, Leeds LS2 9JT, U.K.

[2] Department of Physical Chemistry, University of Valencia, Valencia 46100, Spain

[3] Centre for Computational Chemistry, University of Bristol, Bristol BS8 1TS, U.K.

[4] Air Force Research Laboratory, Kirtland AFB, NM 87117, U.S.A.

Submitted to *J. Chem. Phys.*

April 2012.

Abstract

The first excited electronic state of molecular oxygen, $O_2(a^1\Delta_g)$, is formed in the upper atmosphere by the photolysis of O_3. Its lifetime is over 70 min above 75 km, so that during the day its concentration is about 30 times greater than that of O_3. In order to explore its potential reactivity with atmospheric constituents produced by meteoric ablation, the reactions of Mg, Fe and Ca with $O_2(a)$ were studied in a fast flow tube where the metal atoms were produced either by thermal evaporation (Ca and Mg) or by pulsed laser ablation of a metal target (Fe), and detected by laser induced fluorescence spectroscopy. $O_2(a)$ was produced by bubbling a flow of Cl_2 through chilled alkaline H_2O_2, and its absolute concentration determined from its optical emission at 1270 nm ($O_2(a^1\Delta_g - X^3\Sigma_g^-)$). The following results were obtained at 296 K: $k(Mg + O_2(a) + N_2 \rightarrow MgO_2 + N_2) = (1.8\pm0.2) \times 10^{-30}$ cm^6 molecule^{-2} s^{-1}; $k(Fe + O_2(a) \rightarrow FeO + O) = (1.1\pm0.1) \times 10^{-13}$cm^3 molecule^{-1} s^{-1}; $k(Ca + O_2(a) + N_2 \rightarrow CaO_2 + N_2) = (2.9\pm0.2) \times 10^{-28}$ cm^6 molecule^{-2} s^{-1}; and $k(Ca + O_2(a) \rightarrow CaO + O) = (2.7\pm1.0) \times 10^{-12}$ cm^3 molecule^{-1} s^{-1}. The total uncertainty in these rate coefficients, which mostly arises from the systematic uncertainty in the $O_2(a)$ concentration, is estimated to be ±40%. Mg + $O_2(a)$ occurs exclusively by association on the singlet surface, producing $MgO_2(^1A_1)$, with a pressure dependent rate coefficient. Fe + $O_2(a)$, on the other hand, shows pressure independent kinetics. FeO + O is produced with a probability of only ~ 0.1%. There is no evidence for an association complex, suggesting that this reaction proceeds mostly by near-resonant electronic energy transfer to $Fe(a^5F)$ + $O_2(X)$. The reaction of Ca + $O_2(a)$ occurs in an intermediate regime with two competing pressure dependent channels: (1) a recombination to produce $CaO_2(^1A_1)$, and (2) a singlet/triplet non-adiabatic hopping channel leading to CaO + O(^{3}P). In order to interpret the Ca + $O_2(a)$ results, multireference and density functional theory electronic structure calculations were carried out on the lowest-lying singlet and triplet surfaces. In addition to mapping stationary points, we used a genetic algorithm to locate minimum energy crossing points between the two surfaces. Simulations of the Ca + $O_2(a)$ kinetics were then carried out using a combination of both standard and non-adiabatic RRKM theory implemented within a weak collision, multi-well master equation model. In terms of atmospheric

significance, only in the case of Ca does reaction with $O_2(a)$ compete with O_3 during daytime between 85 and 110 km.

Introduction

The first excited state of molecular oxygen, $O_2(a^1\Delta_g)$, is produced in the mesosphere-lower thermosphere (MLT) region by photolysis of O_3 at wavelengths shorter than 320 nm:[1]

$$O_3 + h\nu \rightarrow O(^1D) + O_2(a^1\Delta_g)$$

$O_2(a)$ is comparatively long-lived in the MLT. The quenching life-time is more than 4 hours,[2] much longer than the phosphorescence lifetime of 73.9 minutes for $O_2(a^1\Delta_g - X^3\Sigma_g^-)$ emission at 1270 nm.[3] Since the rate of O_3 photolysis in the MLT is ~8×10^{-3} s^{-1}, then during daytime the steady-state ratio $[O_2(a)]/[O_3]$ is about 30 [4] and the daytime concentration of $O_2(a)$ around 90 - 100 km is ~ 5×10^9 cm^{-3}. [5] After sunset $O_2(a)$ decays by an order of magnitude every 2.8 hours. $O_2(a)$ contains almost 1 eV of electronic excitation compared with ground-state $O_2(X^3\Sigma_g^-)$, and thus has the potential to be significantly more reactive, although it is not a radical species.

Here we describe a combined experimental and theoretical study of the reactions of $O_2(a)$ with three metallic constituents of the MLT which are produced by the ablation of roughly 50 tonnes of interplanetary dust which enters the atmosphere each day from space.[6] Meteoric ablation gives rise to the permanent layers of metal atoms that occur globally between about 75 and 110 km. Two of these metals – Fe and Ca – have been studied intensively during the last two decades using the ground-based resonance lidar technique.[7] Most recently, satellite-borne spectrometric observations of the earth's dayglow have been used to retrieve the global layer of Mg.[8]

Ca, Mg and Fe atoms all react rapidly with O_3.[9,10] However, given the daytime $[O_2(a)]/[O_3]$ ratio discussed above, the reactions of these metals with $O_2(a)$ could be atmospherically important if their

reaction rate coefficients are larger than about 1×10^{-12} cm^3 molecule^{-1} s^{-1}. This requires the reactions to be exothermic (or very close to thermoneutral). For Mg + O_2(a) there are only two possibilities:

$$Mg(^1S) + O_2(a^1\Delta_g) \rightarrow MgO_2(^1A_1) \qquad \Delta H_0 = -136 \text{ kJ mol}^{-1} \qquad (1a)$$

$$\rightarrow Mg + O_2(^3\Sigma_g^-) \qquad \Delta H_0 = -94 \text{ kJ mol}^{-1} \qquad (1b)$$

where the reaction enthalpies at 0 K are determined using electronic structure calculations (see below) for 1a and experimental energies for 1b.[11] Reaction 1b would involve a spin change which might also allow formation of triplet MgO_2.[12] The Mg-O bond is relatively weak and so formation of MgO + O is endothermic by 164 kJ mol^{-1}. [11] The recombination reaction of Mg with O_2(X) has a barrier of 24 kJ mol^{-1},[12] and thus is extremely slow at room temperature.

For the reaction Fe + O_2(a) there are four possibilities:

$$Fe(a^5D_4) + O_2(a^1\Delta_g) \rightarrow FeO_2(^5A_1) \qquad \Delta H_0 = -376 \text{ kJ mol}^{-1} \qquad (2a)$$

$$\rightarrow Fe(a^5D_4) + O_2(X^3\Sigma_g^-) \qquad \Delta H_0 = -94 \text{ kJ mol}^{-1} \qquad (2b)$$

$$\rightarrow Fe(a^5F_5) + O_2(X^3\Sigma_g^-) \qquad \Delta H_0 = -10 \text{ kJ mol}^{-1} \qquad (2c)$$

$$\rightarrow FeO(^5\Sigma) + O(^3P) \qquad \Delta H_0 = -2\pm20 \text{ kJ mol}^{-1} \qquad (2d)$$

Recombination on the reactant quintet surface could yield FeO_2 (or the inserted OFeO isomer). The large exothermicity shown for 2a refers to formation of the lowest quintet, which actually correlates with Fe + O_2(X).[13] An excited state of quintet FeO_2 should therefore form initially, and a range of triplet and septet states[13] may also be available through spin crossings. In contrast, the reaction between Fe and ground-state $O_2(X^3\Sigma_g^-)$ can only produce FeO_2, but this reaction has a large electronic barrier of about 17 kJ mol^{-1}. [14] Another interesting possibility is near-resonant electronic energy transfer to yield $Fe(a^5F)$ + O_2(X). $Fe(a^5F)$ is the first electronically-excited state of Fe; depending on the a^5F_J multiplet produced this reaction channel ranges from being 10 kJ mol^{-1} exothermic to 4 kJ mol^{-1} endothermic. The final channel producing FeO + O is possibly slightly

exothermic, using a Fe-O bond energy D_0 = 402 kJ mol^{-1}.[15] However, the uncertainty in this bond energy is probably around ±20 kJ mol^{-1}.[16]

Ca + O_2(a) has three potential channels:

$$Ca(^1S) + O_2(a^1\Delta_g) \rightarrow CaO_2(^1A_1) \qquad \Delta H_0 = -322 \text{ kJ mol}^{-1} \qquad (3a)$$

$$\rightarrow Ca + O_2(X^3\Sigma_g^-) \qquad \Delta H_0 = -94 \text{ kJ mol}^{-1} \qquad (3b)$$

$$\rightarrow CaO(^1\Sigma) + O(^3P) \qquad \Delta H_0 = 3\pm17 \text{ kJ mol}^{-1} \qquad (3c)$$

In fact, there is considerable uncertainty in the bond strength of CaO. A fairly recent high level electronic structure study[17] concluded that the bond strength lay in the range 383 to 417 kJ mol^{-1}, so that channel could be endothermic by up to 20 kJ mol^{-1}. Recombination to form $CaO_2(^1A_1)$ (the most stable isomer[18]) is spin-allowed, and may be considerably faster than the recombination of Ca and ground-state O_2(X), which has a barrier of about 6 kJ mol^{-1}.[18] Note that channels 1b and 1c involve a spin crossing from the reactant singlet onto a product triplet surface, which could also allow the formation of triplet CaO_2.[18]

From a theoretical and computational perspective, the kinetics under investigation within this study (in particular, for the Ca + O_2(a) system) present an interesting challenge because they involve spin-hopping processes that occur within an intermediate pressure regime on a multiwell potential energy surface topology. Using a combination of both semiclassical molecular dynamics and statistical mechanics approaches, there has been significant prior work by a number of workers to formulate spin-hopping models which apply in two limits: (1) under zero-pressure, single collision conditions, and (2) under thermal conditions.[19,20] However, far less work has been done to formulate models capable of treating spin-hopping kinetics within intermediate pressure regimes like those characterizing combustion systems or planetary atmospheres. In such regimes, collisionless treatments are inadequate, and explicit semiclassical MD approaches are generally prohibitively expensive. In this work, we extend the multiwell master equation to include non-adiabatic microcanonical spin hopping effects. The net result is a general computational framework model for

polyatomic species which is capable of treating non-adiabatic hopping kinetics that simultaneously occur alongside collisional relaxation processes.

The structure of the paper is as follows. First, we describe the experimental technique used to study the reactions between $O_2(a^1\Delta_g)$ and metal atoms. Second, we determine the experimental kinetics of the reactions 1 - 3. In the final section of the paper, we discuss the microscopic mechanisms that underly the phenomenological kinetics. Within this section, we describe the theoretical/computational approach we have taken in order to simulate the kinetics, including electronic structure calculations and the development of a multiwell spin-hopping master equation.

Experimental technique

Figure 1 is a schematic diagram of the fast flow tube apparatus used to study the kinetics of the Ca, Mg and Fe reactions. The stainless steel flow tube has an internal diameter of 37.5 mm and consists of sections of tube, cross-pieces and nipple sections connected by conflat flanges sealed with copper gaskets. The tube has a total length of 1130 mm from the upstream entry point of the carrier gas to the downstream laser induced fluorescence (LIF) detection cell. Calcium atoms were produced continuously by heating calcium pellets (Aldrich, 99 %) to 1070 - 1120 K. Magnesium atoms were produced by heating magnesium pellets (Aldrich, 99.5 %) to a temperature between 700 and 800 K. The pellets were located in an aluminium oxide crucible placed inside a tungsten basket heater, positioned 1120 mm upstream of the LIF cell. The Ca or Mg atoms were entrained in the main carrier flow of N_2, which entered the tube upstream of the crucible. Ca was detected by resonant LIF at 422.7 nm ($Ca(4^1P_1 - 4^1S)$) using a Nd-YAG-pumped dye laser (pulse rate 10 Hz; pulse energy 10 mJ). Mg was detected by resonant LIF at 285.2 nm ($Mg(3^1P_1 – 3^1S_0)$), after frequency-doubling the dye laser using a BBO crystal.

The source of Fe atoms in the flow tube was the pulsed ablation of a pure iron rod, using a Nd:YAG laser (λ = 532nm, pulse energy = 22 – 31 mJ, repetition rate = 8 Hz). The rod was coupled to a stepper motor (via a vacuum feedthrough in a side-arm of the flow tube), so that the rod could be

rotated (2 - 4 Hz) and also translated slowly. This ensured that a fresh surface of the rod was presented to each successive laser shot, in order to keep the resulting pulses of ablated Fe as uniform as possible. The iron rod was long enough (≈ 5 cm) to project across the central axis of the tube. The laser was loosely focused onto the rod through an orthogonal side-arm, so that the point of ablation was in the centre of the flow tube. The pulse of Fe atoms was then entrained in the N_2 carrier gas and transported downstream to the LIF cell, where the Fe was detected by resonant LIF at 248.3 nm Fe($x^5F^o_5 \leftarrow a^5D_4$).

The reactant flow of $O_2(a)$ in He was injected via a side port downstream of the crucible/ablation cell (Figure 1). The gas flow exited the tube through a throttle valve to a booster pump backed by a rotary pump, providing a volume displacement rate of 110 L s^{-1}. Typically, a total gas flow rate of 3200 sccm was used with pressures ranging from 1 to 10 Torr. The Reynolds number was always below 80, ensuring laminar flow within the tube.

$O_2(a^1\Delta_g)$ was prepared using a new technique,[21,22] where Cl_2 is bubbled through a chilled alkaline solution of H_2O_2:

$$Cl_{2\,(g)} + H_2O_{2\,(aq)} + 2KOH_{(aq)} \rightarrow O_2(a^1\Delta_g) / O_2(X^3\Sigma_g^-)_{\,(g)} + 2KCl_{\,(aq)} + H_2O \qquad (4)$$

This produces $O_2(a^1\Delta_g)$ at up to 30% yield.[21] The $O_2(a)$ generator (Figure 1) consisted of two traps and the optical cell used to monitor 1270 nm emission from $O_2(a)$, all constructed from Pyrex glass. The first trap, containing 60 ml of 35% w/w H_2O_2 held at -21^{o}C, was where reaction 4 took place. 40 ml of chilled 4.0 M KOH was added slowly to this trap to create a slush, through which a 10% Cl_2/He flow was then bubbled at flow rates up to 100 sccm. The second trap, held at -70^{o}C, was used to dry the gas flow by freezing out H_2O. The O_2(a and X)/He flow then entered the cylindrical optical emission cell (length = 100 mm, radius = 10 mm), before flowing through a Teflon valve into the fast flow tube.

The weak emission at 1270 nm from O_2(a-X) emission, exiting through a window at one end of the optical cell, was focused by a lens (bi-convex BK-7 lens, f = 30 mm)) through an interference filter

(centre wavelength = 1270 nm, FWHM = 4.2 nm, peak transmission = 33%) into a glass fibre optic bundle of length 610 mm. The light exiting the bundle was then focused by a second lens onto an InGaAs photodiode detector (Oriel, Model 71671). The photodiode current was read by a pico-ammeter (Keithley). The absolute sensitivity of this optical assembly – light collection, transmission through the fibre optic, and detection – was calibrated using a radiometric calibration standard (Ocean Optics LS-1-CAL NIST-traceable light source).

Experimental Results

Calibration of the $O_2(a)$ flow

Figure 2 shows that the InGaAs photodiode current resulting from 1270 nm emission in the optical cell was always proportional to the Cl_2 concentration entering the first trap of the $O_2(a)$ generator. This implies that a constant fraction of the O_2 produced by reaction 4 was in the $a^1\Delta_g$ state. The calibration of the absolute $O_2(a)$ concentration was achieved in two stages. First, a computer ray-tracing model was developed to determine the total collection efficiency of 1270 nm photons emitted in the gas cell. The model assumed that $O_2(a)$ has a uniform concentration in the emission cell. This should be the case given that the shortest quenching lifetime of $O_2(a)$ caused by the maximum O_2 in the flow in the generator was 42 s,[2] compared with a residence time of the flow in the emission cell of less than 2 s. The model then determined the probability of a photon emitted at each point in the cell being captured by the bi-convex lens and focused through the interference filter onto the entrance of the fibre optic bundle. The total number of photons entering the bundle was then computed by integrating over the cell volume. A correction was applied because the rovibrational line structure of the $O_2(a\text{-}X)$ emission is broader than the bandpass of the interference filter. Convolving the emission spectrum, calculated using PGOPHER [23], with the interference bandpass indicates that only 20.1% of the total emission intensity was transmitted through the filter, compared with the signal which would have been measured if all the emission were at the transmission peak of

the filter. The result is that if the concentration of O_2(a) in the cell were 1.0×10^{16} cm^{-3}, then the O_2(a-X) emission power entering the fibre bundle would be 0.12 nW.

The second stage of the calibration procedure involved replacing the optical cell with the radiometric calibration source. The photodiode current was measured as a function of the distance between the radiometric calibration standard and the collection lens. This showed that the calibration factor was 103 pA nW^{-1}. Hence, a concentration of 1.0×10^{16} cm^{-3} O_2(a) in the cell would produce a photodiode current of 12.4 pA. That is, the calibration factor was 8.1×10^{14} molecule cm^{-3} pA^{-1}.

The right-hand ordinate in Figure 2 shows the resulting O_2(a) concentrations, calculated by applying this calibration factor to the detector current on the left-hand ordinate. The selection of experimental runs shown in Figure 2 covers the range of conversion efficiencies of Cl_2 into O_2(a) observed during the project, which ranged from 16 to 26%. This variation in efficiency seemed most likely due to the cleanliness of the Pyrex glass traps.

Kinetics experiments

Reaction rate coefficients were determined using a procedure we have described in detail elsewhere.[24] Taking reaction 3 as an example, the loss of Ca by diffusion to the flow tube walls and reaction with O_2(a) can be described by a first-order decay coefficient, k', since $[O_2(a)] >> [Ca]$:

$$k' = k_{diff,Ca} + k[O_2(a)] \qquad \text{(E1)}$$

where $k_{diff,Ca}$ describes the loss of Ca by diffusion and k is the rate coefficient for reaction 1 (which may depend on pressure). Experiments were carried out by varying $[O_2(a)]$ while keeping the total mass flow rate and pressure in the flow tube constant. This means that $k_{diff,Ca}$ is constant, as well as the reaction time t between the point of injection of the O_2(a) and the downstream LIF cell. Since the removal of Ca is pseudo first-order,

$$\frac{\ln\left(\frac{[Ca]_0^t}{[Ca]_{O_2(a)}^t}\right)}{t} = \frac{\ln[Ca]_{rel}}{t} = k[O_2(a)] \qquad (E2)$$

where $[Ca]_0^t$ is the concentration at the LIF detection cell in the absence of $O_2(a)$, $[Ca]_{O_2(a)}^t$ is the Ca concentration at the LIF detection cell when $O_2(a)$ is added, and $[Ca]_{rel}$ is the ratio of these concentrations. Plots of $\ln[Ca]_{rel} / t$ versus $[O_2(a)]$ are shown in Figure 3, for a range of pressures in the flow tube. The linear dependence expected from equation II is observed, and the slope of each plot gives the second-order rate coefficient *k*.

Figure 3 shows that reaction 3 is pressure dependent. This is confirmed in Figure 4, which is a plot of *k* against $[N_2]$. The slope of this plot yields the third-order rate coefficient listed in Table I. Note that there is also a significant intercept in Figure 4, which indicates that there is a second-order component to reaction 3. Since the only energetically accessible bimolecular products are CaO + $O(^3P)$ (i.e., channel 3c), this intercept is clear evidence for spin-hopping onto a triplet surface.

Figure 5 illustrates the first-order removal of Fe as a function of $[O_2(a)]$, at two pressures. Note that reaction 2 is essentially independent of pressure. This is confirmed in Figure 6, which also shows the second-order removal rate coefficient for reaction 1 between Mg and $O_2(a)$. The Mg reaction is clearly pressure-dependent although, in contrast to reaction 3 (figure 4), there is not a significant intercept on the ordinate. The rate coefficients for reactions 1 and 2 are also listed in Table I.

A final point to note here is that Mg, Fe and Ca react comparatively slowly with $O_2(X)$. At the highest pressures employed in the flow tube, the reactions of these atoms with $O_2(a)$ are 4020, 116 and 82 times faster than their reactions with ground-state $O_2(X)$ at 300 K, respectively.[12,14,18,25] Therefore, even though the ratio of $O_2(a)/O_2(X)$ entering the flow tube was in some experimental runs as low as 16%, the reactions of these metal atoms with $O_2(X)$ would have had a negligible impact on their removal rates and hence determination of the $O_2(a)$ kinetics.

Discussion and Theoretical Analysis

The experimental results for these three systems show a striking range of kinetic behaviour. On the one hand, the pressure dependence observed for Mg + O_2 is typical of a system in which an association complex undergoes collisional relaxation. On the other hand, for Fe + O_2, the kinetics are pressure independent, suggesting that all relevant kinetic channels involve prompt dissociation. Ca + O_2 lies in between these extremes, with an association complex for which there is a competition between prompt dissociation and collisional stabilization, with non-adiabatic hopping dynamics clearly playing an important role. To provide microscopic insight into the origin of this behaviour, and to formulate kinetics models which allow the laboratory results to be extrapolated over a wider range of conditions, we carried out electronic structure calculations and master equation simulations. This involved a particularly detailed analysis of the Ca + O_2 system, given that it incorporates aspects of both the Mg and Fe kinetics.

The electronic structure calculations, which incorporated both single and multireference approaches, allowed us to map stationary points and dynamically significant regions of the PESs for the experimental systems described above. All single reference approaches utilized hybrid density functional theory (DFT), which includes some exact Hartree-Fock exchange. In particular, we used the B3LYP method along with the 6-311+G(2d,p) triple zeta basis set. This is a large, flexible basis set which has both polarization and diffuse functions. At this level of theory, previous theoretical work estimates an expected uncertainty in the calculated reaction enthalpies on the order of ±20 kJ mol^{-1}.[26] All DFT calculations were performed using the Gaussian 09 suite of programs.[27] The multireference calculations were carried out using MOLPRO,[28] and are described in further detail below.

Our formulation of the multiwell energy-grained master equation (ME) has been described in detail elsewhere,[29,30] so only a brief description is given below. Beginning with a bimolecular A + B type

reaction, the ME allows us to model subsequent adduct formation, isomerisation to form other intermediates, dissociation from the intermediates, and collisional relaxation of the intermediates. The aim of the ME is to provide a description of the reaction system at a macroscopic (or phenomenological) level which is formulated in terms of the behaviour of each of the isomers at an energy resolved (or microcanonical) level. The rovibrational state space of each intermediate is partitioned into 'energy grains' with a width no larger than a few kJ mol^{-1}. A differential rate equation is then constructed to describe the grain populations within each isomer and to model the rates of collisional energy transfer into and out of each grain, as well as the probability that population within each grain undergoes reactive processes. The whole set of coupled differential equations may be expressed in matrix form:

$$\frac{d}{dt}\mathbf{p} = \mathbf{M}\mathbf{p} \qquad \text{(E3)}$$

where **p** is a vector containing the populations, and n_{iE}, of the energy grains. *i* refers to the *i*th isomer and *E* to the energy of the grain belonging to a particular isomer. **M** is the matrix that determines the evolution of grain populations due to collisional energy transfer and reaction. Solution of the matrix equation in (E3) provides the time dependence of **p**, which is of the form:

$$\mathbf{p} = \mathbf{U}e^{\lambda t}\mathbf{U}^{-1}\mathbf{p}(0) \qquad \text{(E4)}$$

where **p**(0) contains the initial (t = 0) conditions for each grain (i.e., $n_{iE}(0)$), **U** is a matrix of eigenvectors obtained from diagonalization of **M**, and $\boldsymbol{\lambda}$ is a vector of the corresponding eigenvalues. The total number of eigenvalues is equal to the number of grains.

All RRKM and ME calculations reported in this work were carried out with the open source master equation program, MESMER (**M**aster **E**quation **S**olver for **M**ulti-well **E**nergy **R**eactions).[31] Microcanonical rate coefficients for adiabatic isomerization and dissociation reactions, $k(E)$, were calculated using RRKM theory as:

$$k(E) = \frac{W(E)}{h\rho(E)} \tag{E5}$$

where $W(E)$ is the sum of states at the transition state, h is Planck's constant, and $\rho(E)$ is the reactant density of states. Non-adiabatic modifications to (E5) for treating singlet to triplet hopping are described below.

Within our formulation of the master equation, collisional energy transfer in the downward direction (i.e., from energy E' to E) was treated using the so-called 'exponential down' model[32] in which:

$$P(E \leftarrow E') = C(E')\exp\left(-\frac{E'-E}{\langle \Delta E_d \rangle}\right) \tag{E6}$$

where $P(E \leftarrow E')$ is the probability of undergoing the downward transition, $C(E')$ is a normalization constant, and $\langle \Delta E_d \rangle$ is the average energy transferred per collision in a downward direction. The transition probabilities describing energy transfer in the upward direction are obtained from those calculated with (E6) and by invoking detailed balance. The exponential down model is an isolated binary collision model that typically calculates collision frequencies from Lennard-Jones parameters describing the intermolecular potentials.

Solution of (E3) yields a full microcanonical description of the system time evolution; however, in order to link the master equation solution to experimental measurements of temperature and pressure dependent rate coefficients, it is generally necessary to transform the microcanonical information included in (E4) to give a phenomenological rate coefficient. In order to accomplish this, we perform an eigenvector/eigenvalue analysis which is similar to methods described by Bartis and Widom.[29,33] The method implemented within MESMER relies on the fact that the eigenvalue spectrum obtained from solution of (E3) generally shows separation between those eigenvalues which describe chemical change, and those which describe relaxation processes.

Finally, we note that the numerical algorithms we use to diagonalize **M** in (E3) are not immune from numerical instabilities – particularly at low temperatures and with very large wells.[34,35] At low

temperatures, numerical instabilities arise from the fact that there is often a very large separation in timescales between those eigenvalues describing chemical change and those describing relaxation. With very large wells, numerical instabilities arise from the fact that the probabilities for energy transfer in the upward direction are often very small. The systems examined in this work are numerically problematic because they involve both relatively low temperatures, and also have very large wells. To limit numerical instabilities, all ME simulations within this work were carried out using high precision arithmetic libraries,[36] which can be called within MESMER using a simple keyword. Additionally, all the results reported in this paper were checked carefully to ensure that they are numerically reliable.

Using the methodology described above, we first discuss our analysis of reaction 1. Figure 7 (top panel) illustrates the stationary points on the singlet potential energy surface for Mg + O_2(a) (red lines), as well as the triplet surface (black lines). If reaction 1 remains on the singlet surface then the outcome should be recombination to form $MgO_2(^1A_1)$ ($r_{Mg\text{-}O}$ = 1.81 Å, $\angle_{O\text{-}Ca\text{-}O}$ = 53.8^o), a well which is 136 kJ mol^{-1} below the reactants. Although there is an Mg-O_2 complex which forms initially on this surface ($r_{Mg\text{-}O}$ = 1.96 Å, $r_{O\text{-}O}$ = 1.31 Å, $\angle_{Mg\text{-}O\text{-}O}$ = 126.7^o), this is 42 kJ mol^{-1} less stable and there is a barrier 67 kJ mol^{-1} higher in energy than $MgO_2(^1A_1)$ between these isomers (i.e., well below the energy of the reactants). The vibrational frequencies and rotational constants of these stationary points are listed in Table II.

Reaction 1 is more than 3 orders of magnitude faster than Mg + O_2(X), which has a significant activation energy of 23 kJ mol^{-1}.[12] Figure 8 illustrates the singlet and triplet surfaces as a function of the distance between the Mg atom and X (the mid-point between the O atoms), and the Mg-X-O angle α. The barrier on the triplet surface (coloured mesh plot) is particularly pronounced as α approaches 0 and 90^o, which accounts for the experimental activation energy.[12] In contrast, there is no barrier on the singlet surface over most angles of approach (monochrome mesh plot). There are no crossing-points between the surfaces at any point below the reactant energy on the singlet surface. Thus, formation of the more stable $MgO_2(^3A_2)$, or dissociation to Mg + O_2(X), should be unlikely.

On this assumption of negligible singlet-triplet crossing, we modelled reaction 1 using MESMER and the molecular parameters in Table II. The internal energy of each stationary point on the PES was divided into a set of energy grains, each with a width of 100 cm^{-1}. The grains associated with Mg-O_2 were then assigned a set of microcanonical rate coefficients for dissociation to Mg + O_2(a), which were determined using an inverse Laplace transformation to link them directly to $k_{rec,\infty}$, the high pressure limiting recombination coefficient.[35,37] For these neutral reactions, $k_{rec,\infty}$ was set to a typical capture rate coefficient of 3×10^{-10} $(T/300\ K)^{1/6}$ cm^3 $molecule^{-1}$ s^{-1},[38] where the small positive temperature dependence is characteristic of a long-range potential governed by dispersion forces. Setting the collisional energy transfer parameters to typical values for an N_2 bath gas ($\langle \Delta E \rangle_{down}$ = 300 cm^{-1},[39] and using MgO_2/N_2 Lennard-Jones parameters of σ = 3.0 Å and ε/k =300 K) yields a phenomenological rate coefficient, k_1(296 K), of 1.5×10^{-30} cm^6 $molecule^{-2}$ s^{-1} (cf. k_1 in Table I), in excellent agreement with the experimental rate coefficient. As shown in Figure 9 (top panel), the only significant product is $MgO_2(^1A_1)$, which forms essentially at the same rate as Mg decays. When 1% of the Mg has reacted with O_2(a), only 0.3% of the product is in the intermediate Mg-O_2 well and this decreases to 0.004% by the time 90% of the Mg has been oxidised.

There are two surprising aspects to the reaction between Fe and O_2(a). The first is that there is no observable pressure dependence to the second-order rate coefficient (Figures 5 and 6), which implies that recombination is negligible (Table I). The second is that the bimolecular channel is comparatively slow. This reaction starts on a quintet surface with the formation of quintet FeO_2. Although the most stable state[13] of quintet FeO_2 is 376 kJ mol^{-1} below the reactants, this state correlates with Fe + O_2(X).[40] Hence, an excited state of quintet FeO_2 should form initially. Time-dependent B3LYP calculations indicate that the lowest-lying quintet FeO_2 which correlates with $Fe(a^5D)$ + O_2(a) is only about 70 kJ mol^{-1} below these reactants, which may account in part for the absence of observable recombination. This state must then rearrange to OFeO, before dissociating to FeO + O,[40] giving rise to the bimolecular reaction observed. Because of the high quintet spin

multiplicity of Fe and FeO, reaction channel 3d may also involve crossing onto surfaces of triplet and septet multiplicities.

Nevertheless, k_2 is relatively small (Table I), about 0.1% of the collision frequency between Fe and O_2(a). This may be because reaction 3d is more endothermic than the ΔH_0 = -2 kJ mol^{-1} which results if D_0(FeO) = 402 kJ mol^{-1}. A value around D_0(FeO) = 388 kJ mol^{-1}, within the range of measured values for this bond energy,[16] would be required. However, another explanation for the small value of k_2 is that quintet FeO_2, which forms initially from Fe + O_2(a), dissociates rapidly to Fe(a^5F) + O_2(X). This channel represents near-resonant energy transfer (ΔE = -10 to +4 kJ mol^{-1}, depending on the Fe spin-orbit multiplet), and is thus likely to be the major channel of reaction 3. The excited Fe(a^5F) atoms produced would be quenched[41] to ground-state Fe(a^5D) in only 6 μs at even the lowest pressure of N_2 used in the flow tube, so this energy transfer reaction would not have been observable as a loss of Fe atoms in the experiment.

In the case of Ca + O_2(a), Figure 7 (bottom panel) illustrates the stationary points on the singlet potential energy surface (red lines), as well as the triplet surface (black lines) which links Ca + O_2(X) with the bimolecular products CaO + O(^{3}P). If reaction 3 remains on the singlet surface, then the outcome should be recombination to form CaO_2($^1A_1$) ($r_{Ca\text{-}O}$ = 1.98 Å, $\angle_{O\text{-}Ca\text{-}O}$ = 45.1^o), a deep well which is 322 kJ mol^{-1} below the reactants. The inserted OCaO($^1A_1$) isomer ($r_{Ca\text{-}O}$ = 2.11 Å, $\angle_{O\text{-}Ca\text{-}O}$ = 133.2^o) is 46 kJ mol^{-1} less stable, and there is a barrier 94 kJ mol^{-1} higher in energy than CaO_2($^1A_1$) between these singlet forms. The vibrational frequencies and rotational constants of these stationary points are listed in Table III.

Perhaps the most interesting feature of reaction 1 is the experimental indication of a dissociation channel, which must correspond to the formation of CaO + O(^{3}P), and thereby requires hopping from the singlet to triplet surface. In an effort to characterize the regions of most likely spin hopping within the Ca+O_2 addition complex, we carried out a number of relaxed multireference CASSCF/cc-pVDZ scans along the O–Ca–O angle. All calculations were performed with a 10 electron, 7 orbital active space consisting of the: (1) in-plane π and π* orbitals on O_2; (2) out-of-plane π and π* orbitals

on O_2; (3) in plane σ and σ* orbitals on O_2 and (4) the Ca 4s orbital (which transforms as A_1 in C2v symmetry). Figure 10 shows the σ and π orbitals used in the CAS calculations along with their corresponding irreducible representations in C_{2v} symmetry. Figure 11 shows relaxed singlet and triplet scans carried out over the OCaO bond angle in each of the C_{2v} symmetries (a_1, a_2, b_1, b_2). For the $^1B_1$ state, results are not shown because we were unable to achieve convergence. For the $^1B_2$ state, the energies are too high to appear on the plot.

An interesting question that arises from the results shown in Figure 11 is why the energy of $^3B_1$ OCaO increases markedly with decreasing OCaO angle, despite the fact its wavefunction symmetry is identical to that of $^3CaO_2$ – i.e., why do the calculations not show a smooth transition to a triplet superoxide leading to Ca + $O_2(X^3\Sigma_g^-)$? This appears to derive from the fact that triplet isomerisation from OCaO to CaO_2, despite the fact that it appears overall symmetry allowed, is forbidden based on the orbital occupation patterns within the different geometries. For Ca + O_2(X) at large separations, inspection of the CI vector obtained in CASSCF calculations shows a lowest energy $^3B_1$ orbital occupation pattern of a_1^2(Ca)-$a_1'^2a_1^2b_1^2b_2^1a_2^1b_2'^0$ (using the orbital labels shown in Figure 10). For OCaO, the $^3B_1$ wavefunction has two dominant electronic configurations, and may be written as 0.52 × a_1^0(Ca)-$a_1'^2a_1^1b_1^1b_2^2b_2'^2a_2^2$ + 0.48 × a_1^0(Ca)-$a_1'^2a_1^2b_1^2b_2^2b_2'^1a_2^1$, both of which differ substantially from the occupation of $^3B_1$ Ca + O_2(X). This is reminiscent of what is observed in O_3,[42] where both the open and cyclic forms have the same overall symmetry, but interconversion is symmetry-forbidden owing to the orbital occupation pattern. In C_s symmetry, a_1 and b_2 orbitals (in C_{2v}) become a′ orbitals, and what were b_1 and a_2 orbitals become a″ orbitals. Hence the orbital occupation of Ca + O_2(X) becomes $a'^2a'^2a'^2a''^2a'^1a''^1a'^0$, giving an overall wavefunction symmetry of $^3A''$. For $^3A''$ OCaO, the occupation pattern is 0.52 × a'^0(Ca)-$a'^2a'^1a''^1a'^2a'^2a''^2$ + 0.48 × a'^0(Ca)-$a'^2a'^2a''^2a'^2a'^1a''^1$. Thus, the conversion of OCaO to Ca + O_2(X) is no longer symmetry forbidden, but there is likely to remain a significant barrier on account of the substantial electron reorganization that takes place on moving from one geometry to the other.

This orbital occupation analysis suggests that any OCaO triplet formed via non-adiabatic hopping from the OCaO singlet will be unlikely to dissociate to Ca + O_2(X). This conclusion is compatible with the experimental observations, which see no evidence for a Ca + O_2(X) channel (which would appear as a slowing down of the Ca removal rate). It is also worth noting that the reaction of Ca + O_2(X) is much slower than Ca + O_2(a) because there is a small barrier (~6 kJ mol^{-1}) in the entrance channel and the well-depth of $CaO_2(^3A_2)$ ($r_{Ca\text{-}O}$ = 2.21 Å, $\angle_{O\text{-}Ca\text{-}O}$ = 35.2°) is shallower,[18] as shown in Figure 7. Hence, the role of Ca + O_2(X) should be limited in these experiments.

The results in Figure 11 show near degeneracy of the singlet and triplet surfaces near OCaO, with an actual singlet-triplet crossing between the $^1A_1$ and $^3B_2$ surfaces. This observation led us to initiate DFT and CASSCF searches for minimum energy crossing points between the $^1A_1$ and $^3B_2$ surfaces in the vicinity of OCaO. The MECP optimization strategy that we utilized in this work builds on a method which relies on defining two orthogonal vectors ***f*** and ***g***:[43,44]

$$f = (E_1 - E_3)\left[\left(\frac{dE_1}{dq}\right) - \left(\frac{dE_3}{dq}\right)\right] = (E_1 - E_3)x_1 \qquad \text{(E7)}$$

$$g = \left(\frac{dE_1}{dq}\right) - \frac{x_1}{|x_1|}\left[\left(\frac{dE_1}{dq}\right)\cdot\frac{x_1}{|x_1|}\right] \qquad \text{(E8)}$$

where q denotes the molecular coordinates, E_1 denotes the energy on the singlet surface, and E_3 the energy on the triplet surface. In the neighbourhood of the MECP, ***f*** is orthogonal to the singlet/triplet crossing seam, and ***g***, which is parallel to the crossing seam, points toward the minimum energy along the seam. At the minimum energy crossing point, both ***f*** and ***g*** vanish.

Typical MECP optimization schemes generally exploit some sort of gradient following in an attempt to minimize ***f*** and ***g***.[43] Instead of taking this approach, we implemented a genetic algorithm to minimize ***f*** and ***g***. This was done for two reasons: (1) gradient following methods were plagued by slow convergence because the OCaO region of the PES is an extremely broad diradical basin with little structure and small energy gradients, and (2) numerical instabilities in our gradient following algorithm (which arose in part from the extremely small OCaO energy gradients) repeatedly

destroyed the molecular C_{2v} symmetry. Utilizing the python PyGene library, we implemented code which interfaced with MOLPRO and Gaussian 09 to undertake an MECP optimization based on simple Mendelian genetics. The 'alleles' that we chose corresponded to the OCaO angle and Ca-O bond distance. The algorithm terminated when $\boldsymbol{f}$ and $\boldsymbol{g}$ met our convergence criteria.

Genetic MECP optimizations were carried out at both the CASSCF and DFT levels of theory, with the DFT description of the $^1A_1$ singlet diradical accomplished using broken spin symmetry. The CASSCF and DFT approaches yielded slightly different MECP geometries. CASSCF gave an MECP with an OCaO angle of 134° and CaO bond distance of 2.17 Å, while DFT searches gave an MECP with an angle of 119° and a bond distance of 2.11 Å. Using the CASSCF methodology described above, we calculated the spin-orbit coupling matrix elements[45] between the $^1A_1$ and $^3B_2$ states at both the DFT and CASSCF MECP geometries. The root mean square of the spin-orbit coupling matrix element is 0.07 cm^{-1} at the CASSCF MECP, whereas it has a value of 1.07 cm^{-1} at the DFT MECP. In the master equation calculations reported below, we examined the sensitivity of our results within this range of spin-orbit coupling values.

Having located the MECPs, we used recently developed code[43,44] to calculate effective vibrational frequencies at the MECP, wherein Hessians for the non-adiabatic states are combined to give an overall effective Hessian within the non-adiabatic crossing seam. After projecting out overall rotations, overall translations, and the gradient for motion orthogonal to the MECP seam,[46] the effective Hessian was mass weighted and diagonalized to provide vibrational frequencies and eigenvectors. Because analytic vibrational frequencies are unavailable for C_{2v} CASSCF wave functions in MOLPRO, we were only able to carry out this vibrational analysis on the DFT geometry. The vibrational analysis clearly shows that the mode corresponding to passage through the MECP seam is the OCaO bend. The MECP vibrational frequencies and rotational constants are given in Table III.

With the above information in hand, we carried out non-adiabatic transition state theory (TST) calculations in MESMER using a modified RRKM expression:[43,47]

$$k(E) = \frac{N_{MECP}(E)}{h\rho(E)} \tag{E9}$$

where $N_{MECP}(E)$ is a convolution of $\rho_{MECP}(E)$, the rigid-rotor/harmonic oscillator density of states at the MECP geometry, and $\rho_{SH}(E)$, the spin-forbidden hopping probabilities, calculated from Landau Zener (LZ) theory:

$$N_{MECP}(E) = \int_0^E \rho_{MECP}(E - E_H) p_{SH}(E) dE_H \tag{E10}$$

where

$$p_{SH}(E_H) = (1+P)(1-P)$$
$$P = \exp\left(\frac{-2\pi V_{ST}^2}{h\Delta F} \sqrt{\frac{\mu}{2(E - E_{MECP})}} \right) \tag{E11}$$

In equation (E11), $\rho_{SH}(E)$ corresponds to a double passage hopping probability, with non-adiabatic transit allowed on both forward and reverse passage through the MECP. V_{ST} is the matrix element for coupling between the two surfaces, μ is the reduced mass for movement along $\boldsymbol{f}$ (31.4 amu) and ΔF is identical to $|x_1|$ (1.06×10^{-3} au $Bohr^{-1}$) in (E8). The LZ surface hopping model is best suited to non-adiabatic systems with localized coupling regions and narrowly avoided crossings, such as that which occurs between the $^1A_1$ and $^3B_2$ surfaces in Figure 11. In addition to this crossing, Figure 11 also shows several weakly coupled states with nearly parallel energy surfaces, for which a Rosen-Zener-Demkov (RZD) type model is best suited to describe the hopping probabilities.[20,48] However, as discussed below, we obtain good agreement with experiment using a model that includes only LZ hopping. Thus we did not additionally include RZD hopping probabilities, although we note that this would be possible.

The MESMER simulations of reaction 3 also required microcanonical rate coefficients for reaction of Ca with O_2(a) to form $CaO_2(^1A_1)$, and for reaction of CaO with O to form ^{3}OCaO. Because these do not have a well defined energy barrier, they were calculated using inverse Laplace transformation[35,37] of the same high pressure limiting rate coefficient as for reaction 2 (see above).

To estimate energy transfer efficiences with N_2, we used values for $\langle \Delta E \rangle_{down}$ and Lennard-Jones parameters which were identical to those discussed above. The phenomenological rate coefficients calculated by MESMER are as follows: $k(Ca + O_2(a) \rightarrow CaO_2) = 3.0 \times 10^{-27}$ cm^6 molecule^{-2} s^{-1} and $k(Ca + O_2(a) \rightarrow CaO + O) = 2.7 \times 10^{-12}$ cm^3 molecule^{-1} s^{-1}, in excellent agreement with experiment (Table I), if the bond energy of CaO is set to D_0 = 385 kJ mol^{-1}. This is 12 kJ mol^{-1} smaller than the recommended value of 397 kJ mol^{-1},[11] although well within the estimated uncertainty of ±17 kJ mol^{-1}.[17] Using the smaller CASSCF spin-orbit coupling constant of 0.07 cm^{-1}, an equally good fit to the experimental data is obtained with D_0 = 391 kJ mol^{-1}. The MESMER estimate of $k(Ca + O_2(a) \rightarrow CaO + O)$ is therefore not very sensitive to the coupling constant, which suggests that D_0 is around 390 kJ mol^{-1}.

Figure 9 (lower panel) shows that the time evolution of the Ca + O_2(a) products is more complex than for Mg + O_2(a), and continues over a much longer timescale than the initial consumption of Ca and production of CaO + O. In addition to singlet OCaO, a major recombination product is triplet OCaO (facilitated by spin hopping), both of which are eventually converted to $CaO_2(^1A_1)$, the most stable of all the possible isomers. Figure 12 illustrates the predicted change with pressure of the overall rate coefficient and the rate coefficients for channels 3a and 3c, and shows good agreement with the measurements over the narrow pressure range achievable in our experimental flow tube. Because k_{3a} is already within 5% of $k_{rec,\infty}$ at a pressure of 10 Torr, this reaction exhibits fall-off behaviour at an unusually low pressure for an atom + diatom recombination reaction. At N_2 pressures below 0.2 Torr, the Ca + O(^{3}P) dissociation channel is "formally direct"[30] – i.e., significantly faster than recombination. In contrast, above 100 Torr, quenching of singlet and triplet OCaO becomes rapid enough that the triplet dissociation channel starts to turn off.

Conclusions

This is the first reported study (to our knowledge) of reactions between metallic atoms and $O_2(a)$. The reactions of Ca, Mg and Fe studied here show strikingly different kinetic behaviour. These metals were chosen for study because of their presence in the earth's upper atmosphere, and the possibility of $O_2(a)$ competing as an oxidant with O_3. It turns out that only reaction with Ca is of atmospheric significance: when $[O_2(a)]$ is about 30 times larger than $[O_3]$ during daytime, the rate of CaO production via $Ca + O_3$ [10] is roughly four times faster than reaction 3. Reactions with Mg and Fe are much too slow to compete with O_3 in the oxidation of Mg and Fe. Nevertheless, these reactions have proved to be of fundamental interest as a test for electronic structure calculations and rate theory, insofar as they have motivated us to formulate a non-adiabatic weak collision Master Equation model for reaction 3, which provides good agreement with the experimental observations. To our knowledge, this study represents one of the first successful fusions of non-adiabatic RRKM theory with a weak collision master equation. Alongside advances in electronic structure theory and our understanding of collisional energy transfer, we believe that this approach will prove useful in future studies where polyatomic non-adiabatic hopping kinetics occur in intermediate pressure regimes.

Acknowledgments

This work was supported through award FA8655-10-1-3045 from the European Office of Aerospace Research and Development. Funding for DRG was provided by the EPSRC Programme Grant EP/G00224X.

References

1 S. M. Ball, G. Hancock, and F. Winterbottom, Faraday Disc. **100**, 215 (1995).

2 K. H. Becker, K. H. Groth, and U. Schurath, Chem. Phys. Lett. **8**, 259 (1971).

[3] S. M. Newman, A. J. Orr-Ewing, D. A. Newnham, and J. Ballard, J. Phys. Chem. A **104** (42), 9467 (2000).

[4] G. P. Brasseur and S. Solomon, *Aeronomy of the Middle Atmosphere*. (Springer, Dordrecht, 2005).

[5] P. P. Batista, H. Takahashi, B. R. Clemesha, and E. J. Llewellyn, J. Geophys. Res. **101** (A4), 7917 (1996).

[6] J. M. C. Plane, Chem. Rev. **103** (12), 4963 (2003).

[7] M. Gerding, M. Alpers, U. von Zahn, R. J. Rollason, and J. M. C. Plane, J. Geophys. Res. **105** (A12), 27131 (2000); T. J. Kane and C. S. Gardner, J. Geophys. Res. **98** (D9), 16875 (1993).

[8] M. Scharringhausen, A. C. Aikin, J. P. Burrows, and M. Sinnhuber, J. Geophys. Res. **113** (D13), article no.: D13303 (2008).

[9] M. Helmer and J. M. C. Plane, J. Chem. Soc. Faraday Trans. **90** (1), 31 (1994); J. M. C. Plane and M. Helmer, Faraday Disc. (100), 411 (1995).

[10] M. Helmer, J. M. C. Plane, and M. R. Allen, J. Chem. Soc. Faraday Trans. **89** (5), 763 (1993).

[11] D. R. Lide, *Handbook of Physics and Chemistry*. (CRC Press, Boca Raton, FL, 2006).

[12] C. F. Nien, B. Rajasekhar, and J. M. C. Plane, J. Phys. Chem. **97** (47), 12422 (1993).

[13] J. M. C. Plane and R. J. Rollason, Phys. Chem. Chem. Phys. **1** (8), 1843 (1999).

[14] M. Helmer and J. M. C. Plane, J. Chem. Soc. Faraday Trans. **90** (3), 395 (1994).

[15] S. Smoes and J. Drowart, High Temp. Sci. **17**, 31 (1984).

[16] R. J. Rollason and J. M. C. Plane, Phys. Chem. Chem. Phys. **2** (10), 2335 (2000).

[17] M. B. Sullivan, M. A. Iron, P. C. Redfern, J. M. L. Martin, L. A. Curtiss, and L. Radom, J. Phys. Chem. A **107** (29), 5617 (2003).

[18] M. L. Campbell and J. M. C. Plane, J. Phys. Chem. A **105** (14), 3515 (2001).

[19] Q. Cui, K. Morokuma, J. M. Bowman, and S. J. Klippenstein, J. Chem. Phys. **110** (19), 9469 (1999); A. W. Jasper, C. Y. Zhu, S. Nangia, and D. G. Truhlar, Faraday Disc. **127**, 1 (2004); J. N. Harvey and M. Aschi, Faraday Disc. **124**, 129 (2003).

[20] E. E. Nikitin, Ann. Rev. Phys. Chem. **50**, 1 (1999).

[21] A. Midey, I. Dotan, and A. A. Viggiano, J. Phys. Chem. A **112**, 3040 (2008).

[22] A. J. Midey, I. Dotan, S. Lee, W. T. Rawlins, M. A. Johnson, and A. A. Viggiano, J. Phys. Chem. A. **111**, 5218 (2007); A. J. Midey, I. Dotan, J. V. Seeley, and A. A. Viggiano, Int. J. Mass Spectrom. **280**, 6 (2009).

[23] C. M. Western, PGOPHER - a Program for Simulating Rotational Structure (University of Bristol).

[24] S. L. Broadley, T. Vondrak, and J. M. C. Plane, Phys. Chem. Chem. Phys. **9** (31), 4357 (2007).

[25] C. Vinckier and P. Christiaens, Bull. Soc. Chim. Belg. **101**, 879 (1992).

[26] J. B. Foresman and A. Frisch, *Exploring chemistry with electronic structure methods*. (Gaussian, Inc., Pittsburgh PA, 1996).

[27] M. J. Frisch, G. W. Trucks, H. B. Schlegel, G. E. Scuseria, M. A. Robb, J. R. Cheeseman, G. Scalmani, V. Barone, B. Mennucci, G. A. Petersson, H. Nakatsuji, M. Caricato, X. Li, H. P. Hratchian, A. F. Izmaylov, J. Bloino, G. Zheng, J. L. Sonnenberg, M. Hada, M. Ehara, K. Toyota, R. Fukuda, J. Hasegawa, M. Ishida, T. Nakajima, Y. Honda, O. Kitao, H. Nakai, T. Vreven, J. J. A. Montgomery, J. E. Peralta, F. Ogliaro, M. Bearpark, J. J. Heyd, E. Brothers, K. N. Kudin, V. N. Staroverov, R. Kobayashi, J. Normand, K. Raghavachari, A. Rendell, J. C. Burant, S. S. Iyengar, J. Tomasi, M. Cossi, N. Rega, J. M. Millam, M. Klene, J. E. Knox, J. B. Cross, V. Bakken, C. Adamo, J. Jaramillo, R. Gomperts, R. E. Stratmann, O. Yazyev, A. J. Austin, R. Cammi, C. Pomelli, J. W. Ochterski, R. L. Martin, K. Morokuma, V. G.

Zakrzewski, G. A. Voth, P. Salvador, J. J. Dannenberg, S. Dapprich, A. D. Daniels, O. Farkas, J. B. Foresman, J. V. Ortiz, J. Cioslowski, and D. J. Fox, *Gaussian 09, Revision A.1*. (Gaussian, Inc., Wallingford CT, 2009).

[28] H.-J. Werner, P. J. Knowles, R. Lindh, F. R. Manby, M. Sch¨utz, P. Celani, T. Korona, G. Rauhut, R. D. Amos, A. Bernhardsson, A. Berning, D. L. Cooper, M. J. O. Deegan, A. J. Dobbyn, F. Eckert, C. Hampel, G. Hetzer, A. W. Lloyd, S. J. McNicholas, W. Meyer, M. E. Mura, A. Nicklass, P. Palmieri, R. Pitzer, U. Schumann, H. Stoll, A. J. Stone, and R. Tarroni, MOLPRO, version 2006.1, a package of ab initio programs, see www.molpro.net.

[29] J. A. Miller and S. J. Klippenstein, J. Phys. Chem. A **110** (36), 10528 (2006); S. H. Robertson, M. J. Pilling, L. C. Jitariu, and I. H. Hillier, Phys. Chem. Chem. Phys. **9** (31), 4085 (2007).

[30] D. R. Glowacki and M. J. Pilling, Chem. Phys. Chem. **11** (18), 3836 (2010).

[31] S. H. Robertson, D. R. Glowacki, C.-H. Liang, C. Morley, R. Shannon, M. Blitz, and M. J. Pilling, MESMER (Master Equation Solver for Multi-Energy Well Reactions), 2008-2012; an object oriented C++ program for carrying out ME calculations and eigenvalue-eigenvector analysis on arbitrary multiple well systems, http: //sourceforge.net/projects/mesmer.

[32] A. W. Jasper and J. A. Miller, J. Phys. Chem. A **115** (24), 6438; J. R. Barker, Int. J. Chem. Kinet. **41** (12), 748 (2009).

[33] J. T. Bartis and B. Widom, J. Chem. Phys. **60** (9), 3474 (1974).

[34] T. J. Frankcombe and S. C. Smith, Theoret. Chem. Acc. **124** (5-6), 303 (2009); K. L. Gannon, D. R. Glowacki, M. A. Blitz, K. J. Hughes, M. J. Pilling, and P. W. Seakins, J. Phys. Chem. A **111** (29), 6679 (2007).

[35] K. L. Gannon, M. A. Blitz, C. H. Liang, M. J. Pilling, P. W. Seakins, and D. R. Glowacki, J. Phys. Chem. A **114** (35), 9413.

[36] Y. Hida, X. S. Li, and D. H. Bailey, Arithmetic **15** (2000).

[37] J. W. Davies, N. J. B. Green, and M. J. Pilling, Chem. Phys. Lett. **126** (3-4), 373 (1986).

[38] Y. Georgievskii and S. J. Klippenstein, J. Chem. Phys. **122**, art. no. 194103 (2005).

[39] R. G. Gilbert and S. C. Smith, *Theory of Unimolecular and Recombination Reactions*. (Blackwell, Oxford, 1990).

[40] D. E. Self and J. M. C. Plane, Phys. Chem. Chem. Phys. **5**, 1407 (2003).

[41] S. A. Mitchell and P. A. Hackett, J. Chem. Phys. **93**, 7813 (1990).

[42] S. S. Xantheas, G. J. Atchity, S. T. Elbert, and K. Ruedenberg, J. Chem. Phys. **94** (12), 8054 (1991).

[43] J. N. Harvey and M. Aschi, Phys. Chem. Chem. Phys. **1** (24), 5555 (1999).

[44] N. Koga and K. Morokuma, Chem. Phys. Lett. **119** (5), 371 (1985).

[45] A. Berning, M. Schweizer, H. J. Werner, P. J. Knowles, and P. Palmieri, Molec. Phys. **98** (21), 1823 (2000).

[46] W. H. Miller, N. C. Handy, and J. E. Adams, J. Chem. Phys. **72** (1), 99 (1980).

[47] K. L. Gannon, M. A. Blitz, C. H. Liang, M. J. Pilling, P. W. Seakins, D. R. Glowacki, and J. N. Harvey, Faraday Disc. **147**, 173.

[48] A. W. Jasper, M. D. Hack, and D. G. Truhlar, J. Chem. Phys. **115** (4), 1804 (2001).

[49] K. P. Huber and G. Herzberg, in *NIST Chemistry WebBook, NIST Standard Reference Database Number 69*, edited by P. J. Linstrom and W. G. Mallard (National Institute of Standards and Technology, Gaithersburg MD, 2012), pp. http: //webbook.nist.gov.

Table I. Rate coefficients measured in the present study at 296 K. The quoted uncertainties are the standard errors from kinetics plots such as in Figures 3 and 5. The total uncertainty, which mostly arises from the systematic uncertainty in the $O_2(a)$ concentration, is estimated to be ±40%.

Reaction	Bimolecular Rate Coefficient cm^3 $molecule^{-1}$ s^{-1}	Termolecular Rate Coefficient cm^6 $molecule^{-2}$ s^{-1}
$Mg + O_2(a)$	$< 2.4 \times 10^{-14}$	$(1.8\pm0.2) \times 10^{-30}$
$Ca + O_2(a)$	$(2.7\pm1.0) \times 10^{-12}$	$(2.9\pm0.2) \times 10^{-28}$
$Fe + O_2(a)$	$(1.1\pm0.1) \times 10^{-13}$	$< 2.4 \times 10^{-31}$

Table II. RRKM parameters for $Mg + O_2(a)$

Species	Vibrational frequencies[a]	Rotational constants[a]	Relative energy[b]
$MgO_2(^1A_1)$ [c]	575, 667, 831	0.783, 0.471, 0.294	0
TS from $Mg\text{-}O_2(^1A')$ to $MgO_2(^1A_1)$ [c]	320*i*, 592, 960	1.286, 0.297, 0.241	67
$Mg\text{-}O_2(^1A')$ [c]	240, 430, 1148	3.194, 0.192, 0.181	42
$Mg + O_2(a)$ [d]	1484	1.426	136

[a] In cm^{-1}; [b] kJ mol^{-1}; [c] calculated at the B3LYP/6-311+g(2d,p) level of theory; [d] NIST Webbook[49]

Table III. RRKM parameters for Ca + O_2(a)

Species	Vibrational frequencies[a]	Rotational constants[a]	Relative energy[b]
$CaO_2(^1A_1)$ [c]	501, 622, 807	0.914, 0.284, 0.217	0
TS from $CaO_2(^1A_1)$ to $OCaO(^1A_1)$ [c]	260*i*, 506, 618	0.400, 0.338, 0.183	94
$OCaO(^1A_1)$ [c]	106, 468, 532	1.355, 0.141, 0.128	46
$OCaO(^3B_2)$ [c]	103, 466, 521	1.460, 0.139, 0.127	45
MECP from $OCaO(^1A_1)$ to $OCaO(^3B_2)$ [c]	545, 458	0.834, 0.161, 0.135	59
Ca+ O_2(a) [d]	1484	1.426	322
CaO + O [d]	732	0.445	328 – 334[e]

[a] In cm^{-1}; [b] kJ mol^{-1}; [c] calculated at the B3LYP/6-311+g(2d,p) level of theory; [d] NIST Webbook[49]; [e] fitted range (see text)

Figure Captions

Figure 1. Schematic diagram of the $O_2(a)$ generator coupled to a fast flow with laser induced fluorescence detection for studying metal atom reactions (exemplified by Mg) with $O_2(a^1\Delta_g)$

Figure 2. $O_2(a)$ emission current measured with the In-Ga-As detector at 1270 nm, as a function of $[Cl_2]$ in the generator. The corresponding calibrated $[O_2(a)]$ is shown on the right-hand ordinate. Data from a selection of experimental runs over several months shows that the efficiency for $O_2(a)$ production ranged from 16 – 26% of the Cl_2.

Figure 3. Kinetic plots showing the first-order removal rate of Ca as a function of $[O_2(a)]$, at five different pressures of N_2 in the flow tube.

Figure 4. Plot of the second-order rate coefficient for Ca + $O_2(a)$ as a function of N_2 concentration. This reaction exhibits third-order (pressure) dependence demonstrating the formation of $CaO_2(^1A_1)$; the significant intercept indicates that the bimolecular channel to CaO + O is also active.

Figure 5. Kinetic plots showing the first-order removal rate of Fe as a function of $[O_2(a)]$, at two different pressures of N_2 in the flow tube.

Figure 6. Plot of the second-order rate coefficient for Mg + $O_2(a)$ and Fe + $O_2(a)$ as a function of $[N_2]$. The Mg reaction exhibits third-order kinetics forming $MgO_2(^1A_1)$. The Fe reaction shows no pressure dependence, indicating the formation of FeO + O is the only reactive channel.

Figure 7. Potential energy curves (calculated at the B3LYP/6-311+g(2d,p) level of theory) for: Mg + $O_2(a)$ (top panel); and Ca + $O_2(a)$ (bottom panel). Singlet surfaces are shown by red lines and triplet surfaces by black lines. For Mg + $O_2(a)$, the only product is $MgO_2(^1A_1)$. Recombination of Ca + $O_2(a)$ produces mostly $CaO_2(^1A_1)$. However, there is a non-adiabatic crossing seam between $OCaO(^1A_1)$ and $OCaO(^3B_2)$, where there is a small probability of switching onto the triplet surface and generating the bimolecular products CaO + $O(^3P)$.

Figure 8. Potential energy surfaces for Mg + O_2(a) (monochrome shading) and Mg + O_2(X) (coloured shading), calculated at the B3LYP/6-311+g(2d,p) level of theory. The diagram illustrates that there are no intersections between the surfaces. Thus, the only possible reaction of Mg with O_2(a) is recombination to $MgO_2(^1A_1)$.

Figure 9. Time-resolved concentration profiles predicted by MESMER. Top panel: Mg + O_2(a), $[O_2(a)] = 1.0 \times 10^{14}$ cm^{-3}; $[N_2] = 3.2 \times 10^{17}$ cm^{-3}. Bottom panel: Ca + O_2(a), $[O_2(a)] = 5.0 \times 10^{12}$ cm^{-3}; $[N_2] = 3.9 \times 10^{16}$ cm^{-3}.

Figure 10. π and σ orbitals used to carry out the CASSCF calculations described in the text. The left and right hand side of the figure shows the orbitals as they appear in OCaO and CaO_2, respectively. Each orbital configuration is also identified by the corresponding symmetry label of its irreducible representation within the C_{2v} point group. The last set of orbitals, a_1' and b_2', are labelled using a prime (′) only to distinguish them from the top set of orbitals, which have the same symmetries.

Figure 11. Relaxed CASSCF potential energy scans along the OCaO angle. As discussed in the text, $^1B_1$ and $^1B_2$ are not shown. There is a crossing between $^1A_1$ and $^3B_2$, and the triplet surfaces all increase rapidly to very high energies instead of evolving smoothly to a $^3CaO_2$ superoxide type structure.

Figure 12. Modelled dependence of the rate coefficients for the reaction of Ca with O_2(a) to form $CaO_2(^1A_1)$ (dash-dot line) or CaO + O (dash line), as a function of N_2 concentration. The total rate coefficient (solid line) is compared with the rate coefficients measured in the present study.

Figure 1.

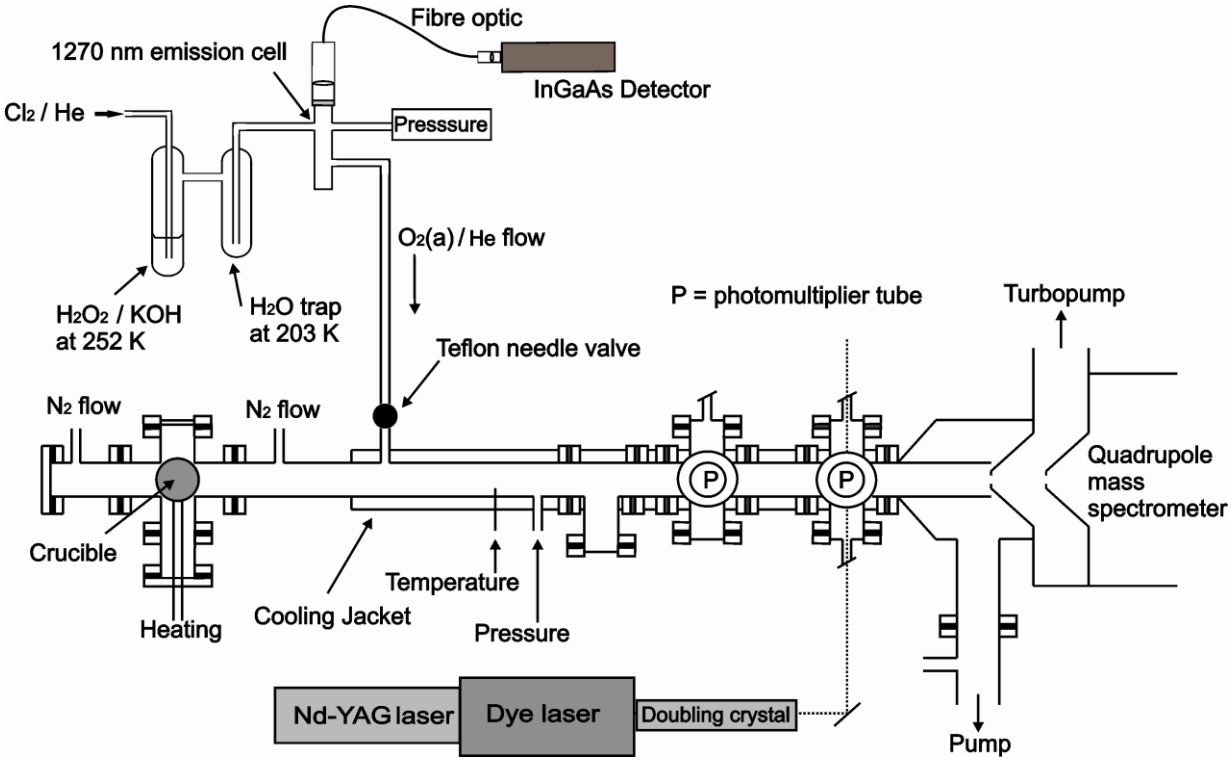

Figure 1. Schematic diagram of the $O_2(a)$ generator coupled to a fast flow with laser induced fluorescence detection for studying metal atom reactions (exemplified by Mg) with $O_2(a^1\Delta_g)$

Figure 2.

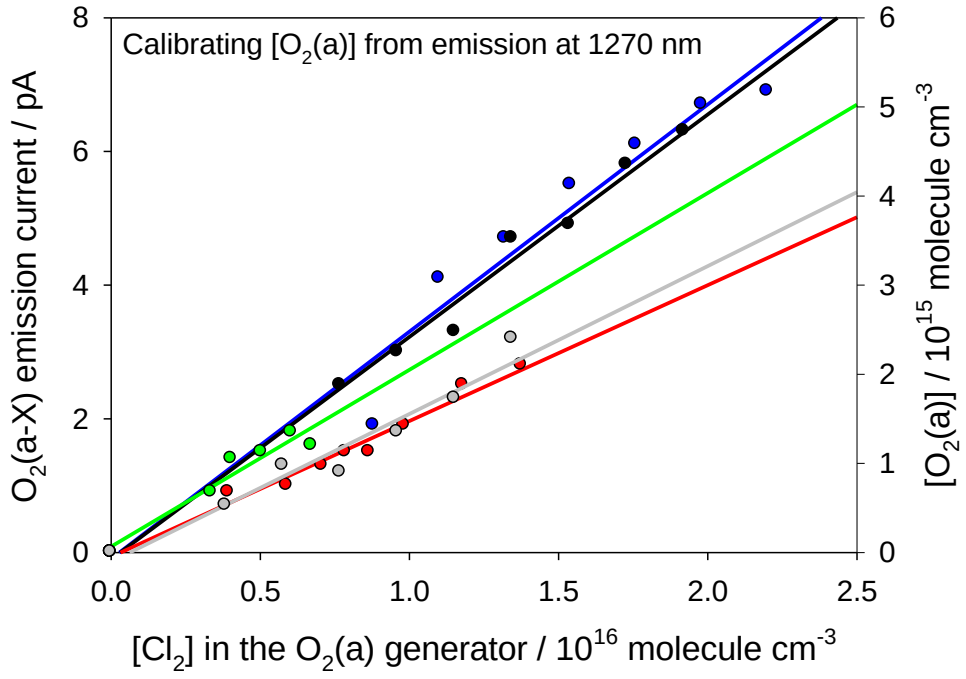

Figure 2. $O_2(a)$ emission current measured with the In-Ga-As detector at 1270 nm, as a function of $[Cl_2]$ in the generator. The corresponding calibrated $[O_2(a)]$ is shown on the right-hand ordinate. Data from a selection of experimental runs over several months shows that the efficiency for $O_2(a)$ production ranged from 16 – 26% of the Cl_2.

Figure 3.

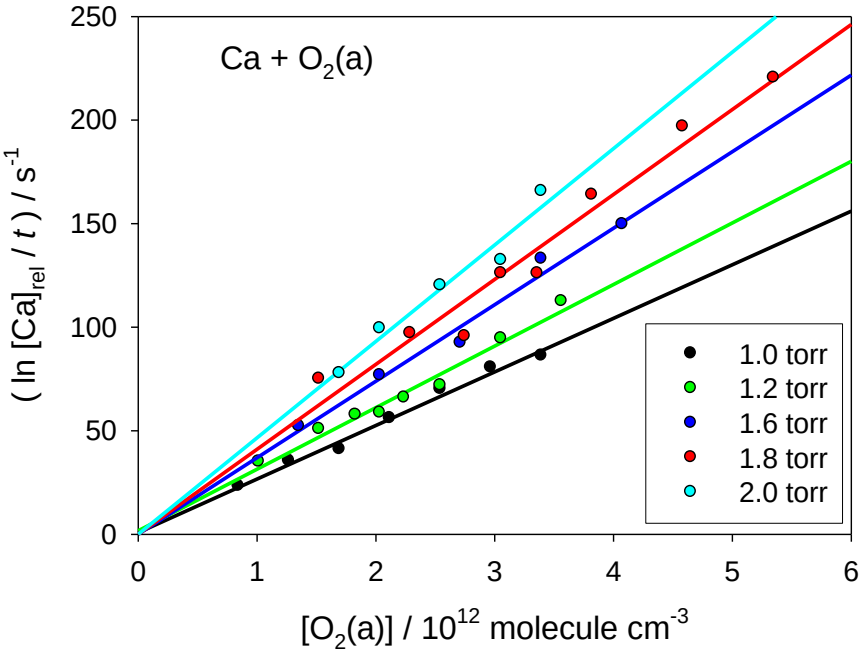

Figure 3. Kinetic plots showing the first-order removal rate of Ca as a function of $[O_2(a)]$, at five different pressures of N_2 in the flow tube.

Figure 4.

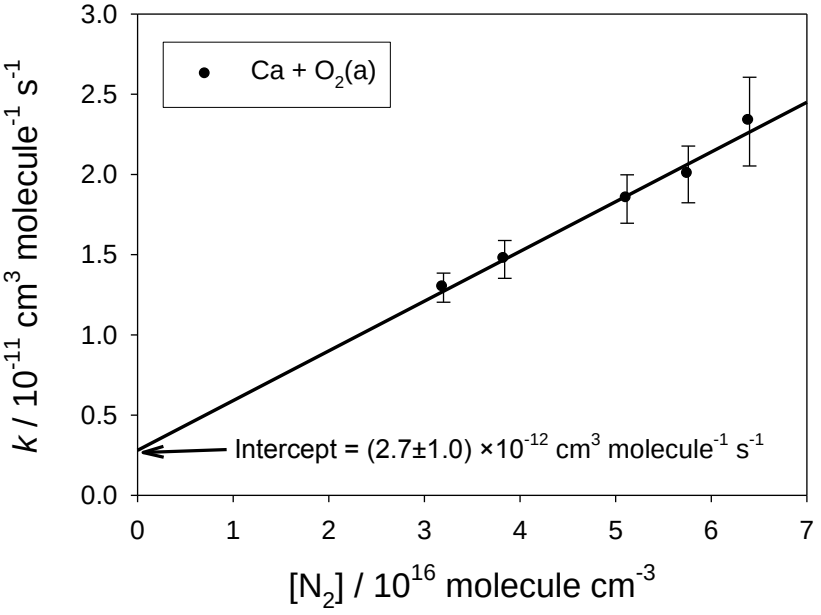

Figure 4. Plot of the second-order rate coefficient for Ca + O_2(a) as a function of N_2 concentration. This reaction exhibits third-order (pressure) dependence demonstrating the formation of $CaO_2(^1A_1)$; the significant intercept indicates that the bimolecular channel to CaO + O is also active.

Figure 5.

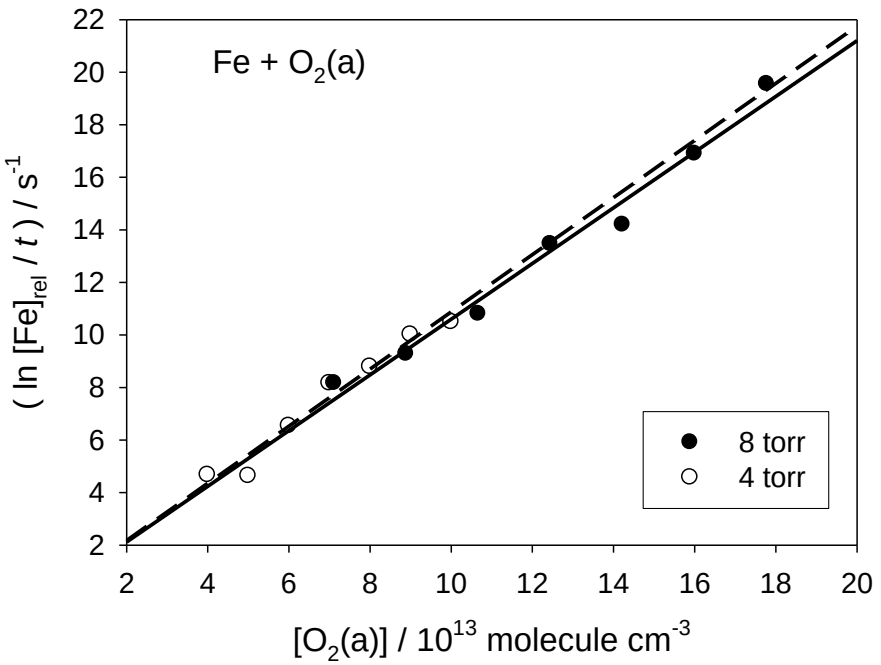

Figure 5. Kinetic plots showing the first-order removal rate of Fe as a function of $[O_2(a)]$, at two different pressures of N_2 in the flow tube.

Figure 6.

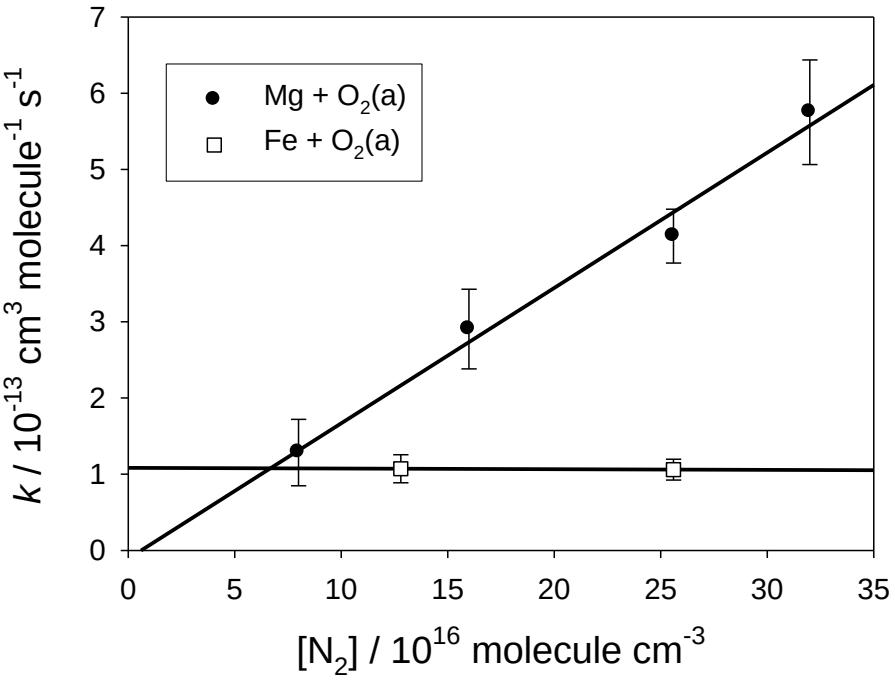

Figure 6. Plot of the second-order rate coefficient for Mg + O_2(a) and Fe + O_2(a) as a function of [N_2]. The Mg reaction exhibits third-order kinetics forming $MgO_2(^1A_1)$. The Fe reaction shows no pressure dependence, indicating the formation of FeO + O is the only reactive channel.

Figure 7.

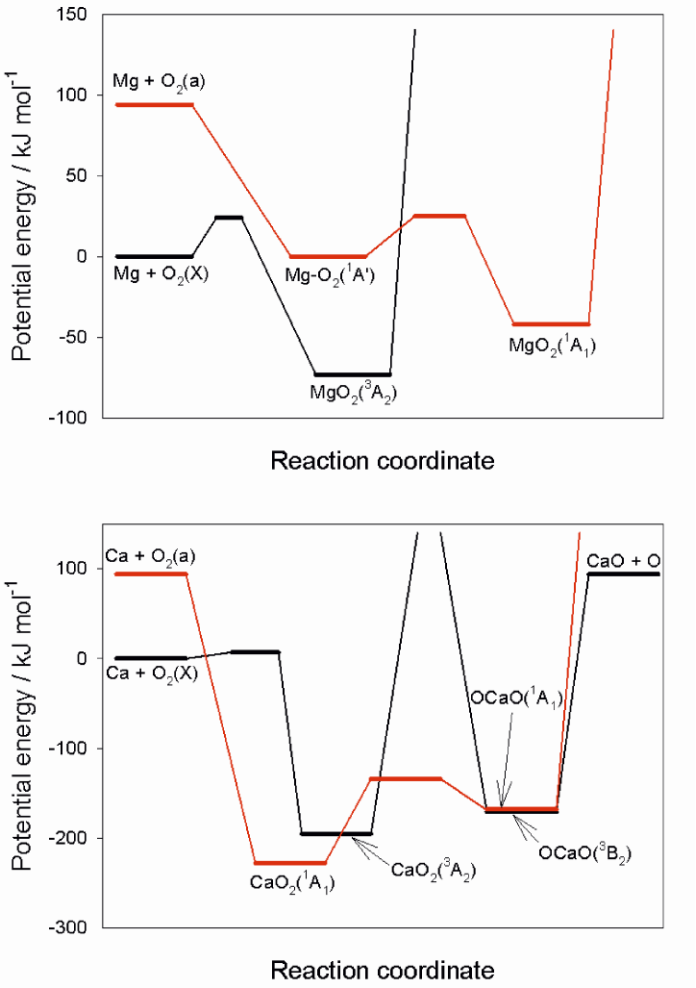

Figure 7. Potential energy curves (calculated at the B3LYP/6-311+g(2d,p) level of theory) for: Mg + O_2(a) (top panel); and Ca + O_2(a) (bottom panel). Singlet surfaces are shown by red lines and triplet surfaces by black lines. For Mg + O_2(a), the only product is $MgO_2(^1A_1)$. Recombination of Ca + O_2(a) produces mostly $CaO_2(^1A_1)$. However, there is a non-adiabatic crossing seam between $OCaO(^1A_1)$ and $OCaO(^3B_2)$, where there is a small probability of switching onto the triplet surface and generating the bimolecular products CaO + $O(^3P)$.

Figure 8.

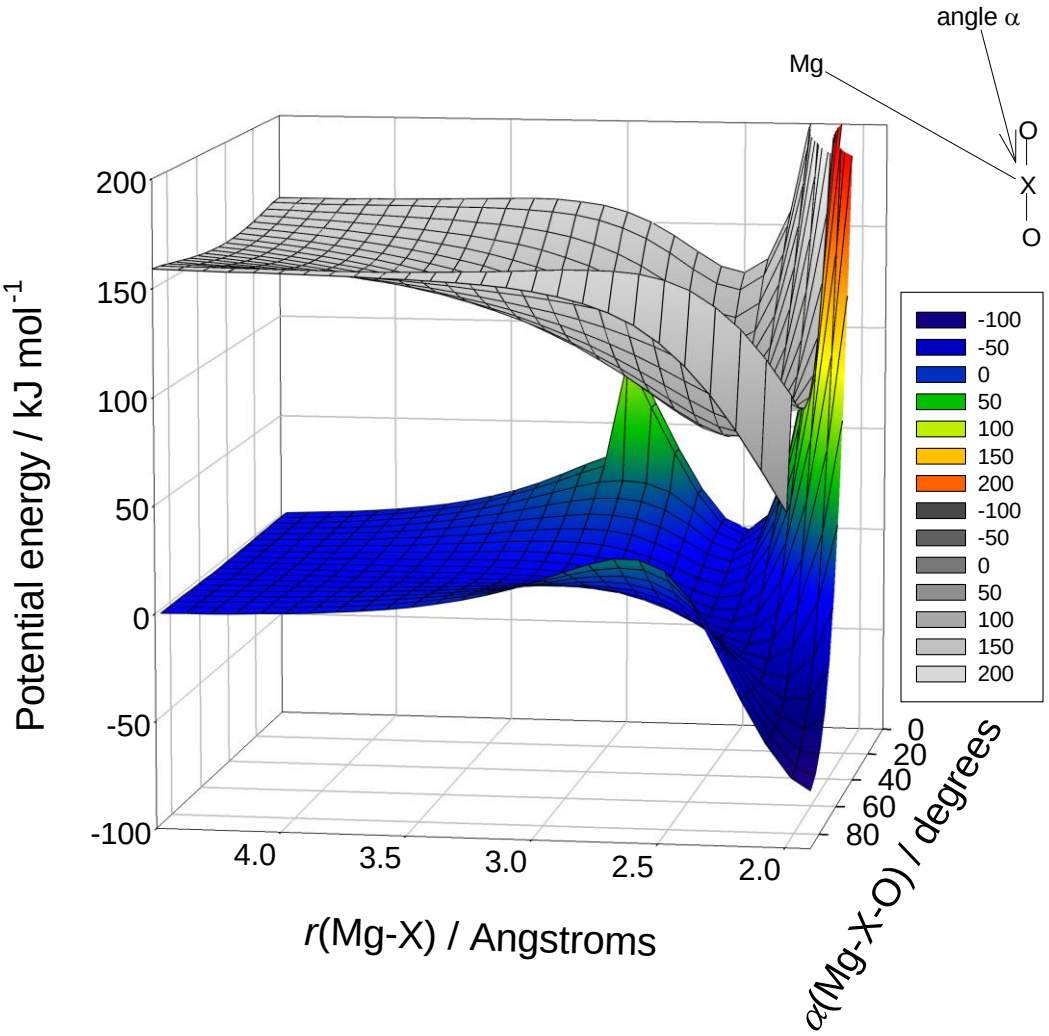

Figure 8. Potential energy surfaces for Mg + O_2(a) (monochrome shading) and Mg + O_2(X) (coloured shading), calculated at the B3LYP/6-311+g(2d,p) level of theory. The diagram illustrates that there are no intersections between the surfaces. Thus, the only possible reaction of Mg with O_2(a) is recombination to $MgO_2(^1A_1)$.

Figure 9.

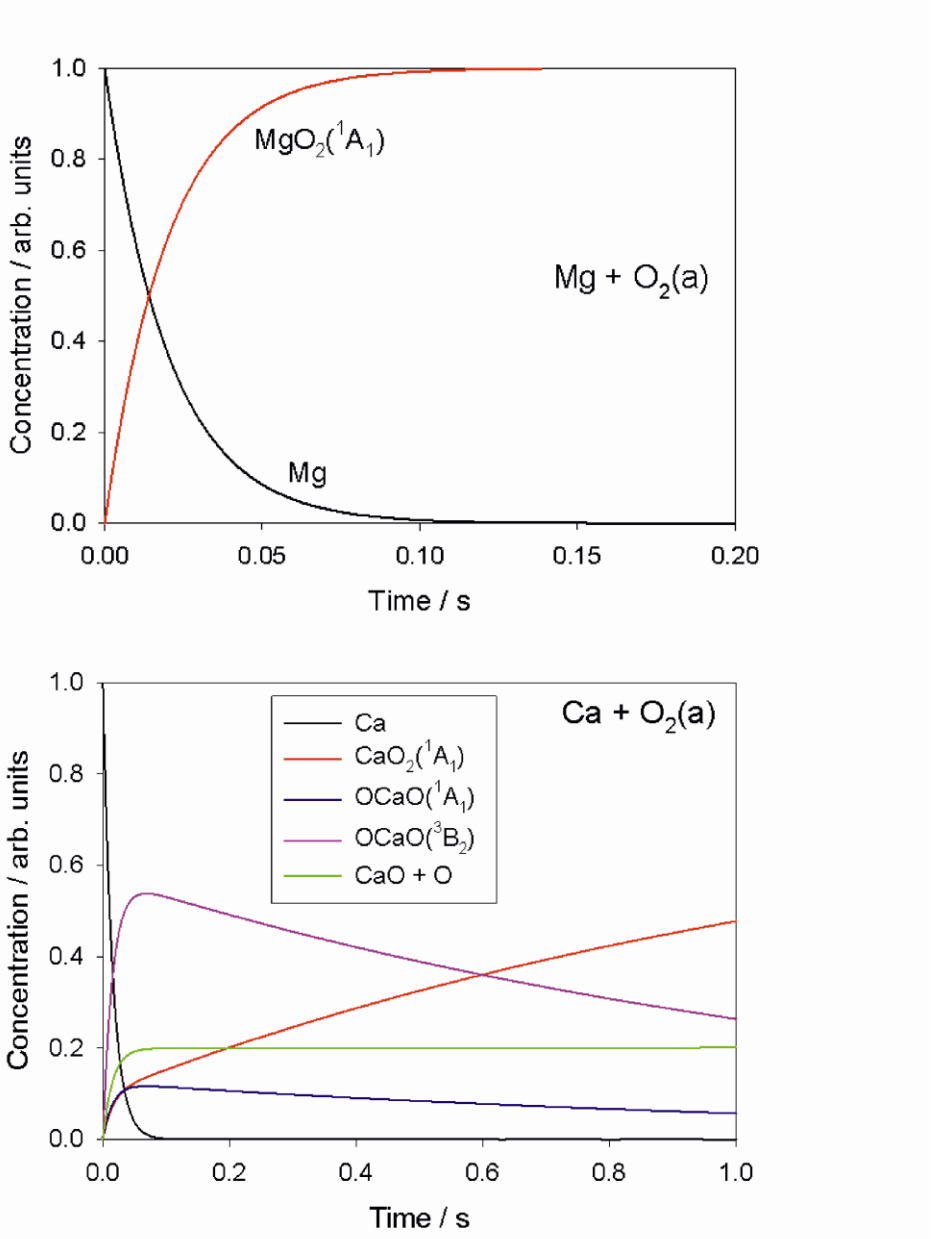

Figure 9. Time-resolved concentration profiles predicted by MESMER. Top panel: Mg + O_2(a), [O_2(a)] = 1.0 × 10^{14} cm^{-3}; [N_2] = 3.2 × 10^{17} cm^{-3}. Bottom panel: Ca + O_2(a), [O_2(a)] = 5.0 × 10^{12} cm^{-3}; [N_2] = 3.9 × 10^{16} cm^{-3}.

Figure 10

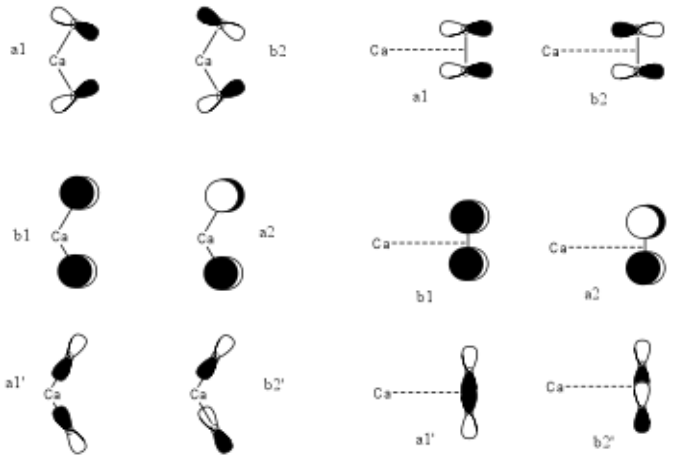

Figure 10. π and σ orbitals used to carry out the CASSCF calculations described in the text. The left and right hand side of the figure shows the orbitals as they appear in OCaO and CaO_2, respectively. Each orbital configuration is also identified by the corresponding symmetry label of its irreducible representation within the C_{2v} point group. The last set of orbitals, a_1' and b_2', are labelled using a prime (′) only to distinguish them from the top set of orbitals, which have the same symmetries.

Figure 11

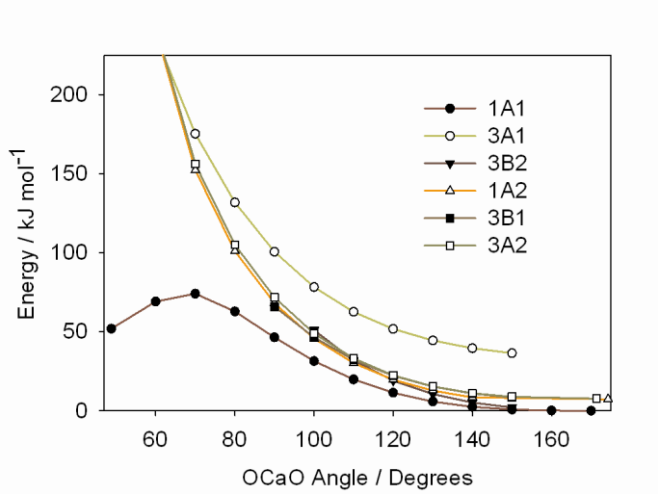

Figure 11. Relaxed CASSCF potential energy scans along the OCaO angle. As discussed in the text, $^1B_1$ and $^1B_2$ are not shown. There is a crossing between $^1A_1$ and $^3B_2$, and the triplet surfaces all increase rapidy up to very high energies instead of evolving smoothly to a $^3CaO_2$ superoxide type structure.

Figure 12.

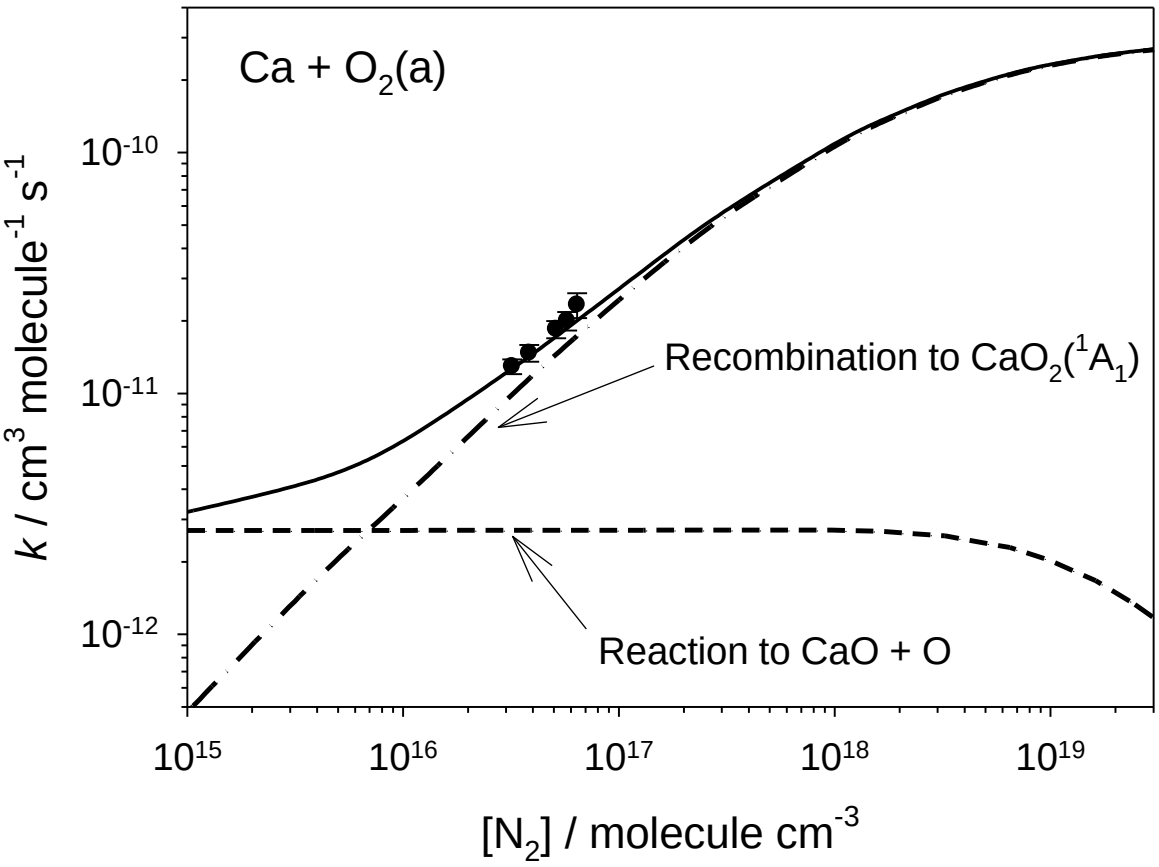

Figure 12. Modelled dependence of the rate coefficients for the reaction of Ca with O_2(a) to form $CaO_2(^1A_1)$ (dash-dot line) or CaO + O (dash line), as a function of N_2 concentration. The total rate coefficient (solid line) is compared with the rate coefficients measured in the present study.